

**Experimental measurement of two copropagating shocks interacting with an unstable interface**

C. A. Di Stefano <sup>\*</sup>, F. W. Doss, E. C. Merritt, B. M. Haines , T. R. Desjardins, B. G. DeVolder,  
K. A. Flippo, L. Kot, H. F. Robey, and D. W. Schmidt   
*Los Alamos National Laboratory, Los Alamos, New Mexico 87545, USA*

M. Millot   
*Lawrence Livermore National Laboratory, Livermore, California 94550, USA*

 (Received 6 February 2020; accepted 10 September 2020; published 23 October 2020)

In this work, we present results from experiments capable of producing and measuring the propagation of multiple successive, copropagating shocks across an unstable planar interface, where the shocks are independently driven and separately controllable, enabling the study of this important phenomenon. Copropagating shocks play a significant role in a wide range of systems involving stratified media subject to a shock, and exhibit different physical characteristics compared to counterpropagating shocks. Existing techniques, however, preclude copropagating shocks, so experiments to date have been limited to the study of counterpropagating shocks. We address this previous limitation and open a physical parameter space for study using a new hohlraum platform on the National Ignition Facility. Initial experimental results are presented together with comparisons from numerical simulations.

DOI: [10.1103/PhysRevE.102.043212](https://doi.org/10.1103/PhysRevE.102.043212)

Successive, copropagating shocks interacting with an unstable interface are ubiquitous in inertial confinement fusion (ICF), where they are essential components of structured indirect drive concepts [1], and other high-energy-density (HED) experiments. They are therefore of great practical importance, yet to our best knowledge have never before been experimentally isolated and studied. In the context of ICF, they appear in converging, integrated environments, while in planar systems they are often the product of uncontrollable reflections [2,3], and researchers have been forced to rely on unvalidated computations and theory to understand their contribution to the behaviors of these systems. In this report, we present experiments measuring such shocks, where each shock is driven separately and can be controlled on its own, using an experimental capability involving hybrid laser direct-indirect drive into a hohlraum. We then demonstrate a computational design strategy able to predict the nontrivial physics of the dynamically-evolving hohlraum. This represents a pivotal advance, establishing the basis for the study of this important, unexplored parameter space.

A significant body of experimental and computational literature [4] does exist on the effects of *counterpropagating* reshocks—an already formidable nonlinear problem—yet this is of limited applicability to *copropagating* shocks since the physics of shock interactions in each direction and at a static or evolving interface are different. Copropagating shocks have unique outcomes [5–7] compared to the counterpropagating reshock, due to the asymmetric nature of several physical properties of shock interactions with interfaces, and which

to our best knowledge have never before been isolated in the laboratory.

As a simple simulated example, consider the phase reversal of a sinusoidal interface perturbation (initially heavy-to-light) under the action of two strong shocks carrying equal energy. Figure 1 compares the Richtmyer-Meshkov growth of such a perturbation when the shocks are copropagating versus counterpropagating. The results are purposefully nondimensionalized to emphasize that the key, broadly-applicable physics are the shock direction, not the choice of any particular interface structure. As shown in the figure, the counterpropagating case grows significantly more than the copropagating case with one fewer phase inversion, though if the interface were reversed, the opposite would occur. Existing experimental techniques (e.g., gas dynamic shock tubes or even existing HED platforms) can produce the *counterpropagating* case (red curve) but fail to allow demonstration of the *copropagating* case (black curve). The unique way in which experiments can be driven on HED facilities allows us to now address such gaps in our understanding, by using a novel hohlraum to generate two independent, separately controllable shocks and measuring the resulting hydrodynamics. This enables future research to underpin a broad and otherwise incomplete set of possibilities of shock hydrodynamics in such experiments, previously inaccessible to researchers. Further, although this capability was conceived for the NIF, it should also be of worldwide relevance, and applicable to a number of recent and upcoming research facilities in its class, including the Laser Mégajoule and Extreme Light Infrastructure facilities in Europe, the ISKRA-6 in Russia, and the Shenguan-IV in China.

We produce these copropagating shocks using a planar ablator of iodinated plastic (3% atomic iodine composition)

<sup>\*</sup>carlosds@lanl.gov

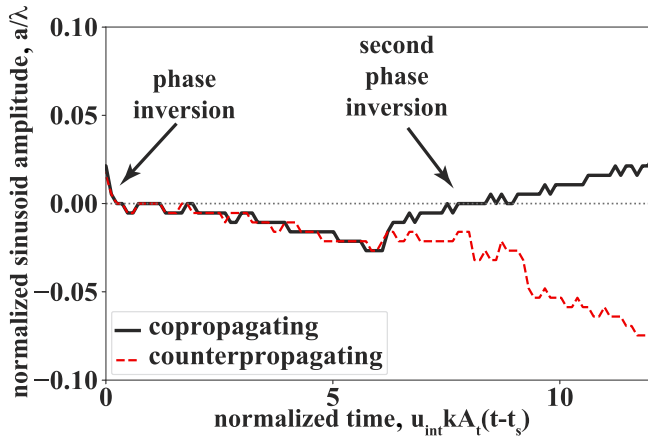


FIG. 1. Simulated comparison of the growth rate, which is dramatically different and includes an extra phase shift, of a sinusoid subject to two copropagating shocks of equal energy, compared to the equivalent counterpropagating case. The amplitude  $a$  is normalized by the wavelength  $\lambda$ ; the time  $t$  is normalized by the postshock interface velocity  $u_{\text{int}}$ , the wave number  $k$ , the Atwood number  $A_t$ , and the shock crossing time  $t_s$ .

with a density of  $1.48 \text{ g/cm}^3$ , placed across the radiation exit hole (REH) of a cylindrical gold halfraum, as shown in Fig. 2(a). A halfraum is conceptually similar to a hohlraum except that lasers enter the open cylinder from one end only instead of both, such that the object to be indirectly irradiated lies at the other end (the REH) of the cylinder instead of within it. This setup is adapted from the Shock/Shear [8] design for the NIF. The halfraum is 4 mm in diameter and 3 mm long, and the primary difference between this and the Shock/Shear halfraum is that the laser entrance hole (LEH) has been expanded to allow entry of the direct-drive beams. Meanwhile, the configuration for the indirect drive remains unchanged from the Shock/Shear drive, and the pulse is timed to begin with some delay after the beginning of the direct-drive pulse (in the case of the data described here, the delay is 3 ns). A diagram of the angles of incidence of the beams into the halfraum is shown in Fig. 2(b), while the pulse shape is

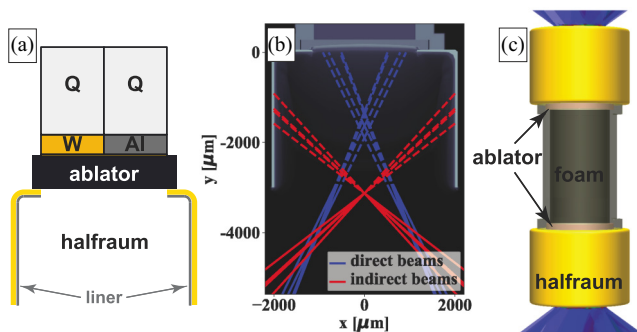


FIG. 2. (a) Sketch of the experimental system. (b) Diagram showing the incidence of the direct- and indirect-drive laser beams on the ablator and halfraum walls, respectively, for the halfraums shown in the next two frames. (c) Sketch of the variation of the system for imaging measurements.

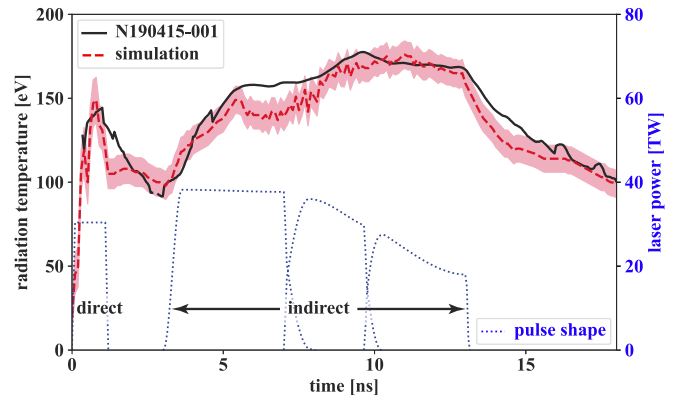


FIG. 3. Radiation temperature measurement made by the Dante diagnostic, for NIF shot N190415-001, shown as a solid black curve. An estimated prediction from the simulation is included, as a red dashed curve. The laser pulse shape is shown as a dotted blue curve. The simulation predicts the temperature to within a few eV for most of the duration of the experiment.

shown as the dotted blue curves in Fig. 3. A key complication is the behavior of the hohlraum as it dynamically fills with plasma, in the delay between the two pulses. An important feature in permitting the second shock is an approximately  $10 \mu\text{m}$  parylene-N (chemically, CH) coating on the halfraum interior, resulting in a low- $Z$  CH plasma fill rather than gold.

To model the system, we use the xRAGE code, a branch of the adaptive-grid, Eulerian radiation-hydrocode RAGE [9] maintained by Los Alamos National Laboratory. The code includes packages for multigroup radiation diffusion, laser ray tracing, a three-temperature plasma model, thermonuclear burn, electron (including nonlocal [10]) conduction and ion conduction, and tabular equations of state (EOS). An important aspect of correctly predicting the shock physics is the use of a laser model [11,12], adapted from the Mazinisin laser package in the DRACO code [13] and implemented in xRAGE. This model allows us to separate out physics effects on the energy deposition that might otherwise be swept into tuning multipliers, impacting our predictive capacity for future platform modifications. Further, performing the simulations in two dimensions, despite the one-dimensional-like behavior of the shocks, allows us to treat the physics occurring in the halfraum with some fidelity. Equations of state are taken from the SESAME [14,15] database, where we treat any undoped plastic as polystyrene, and the doped plastic as an ideal gas mixture of carbon, hydrogen, and a xenon surrogate in place of iodine (the latter does not have a SESAME EOS). We expect this to be reasonable, since the laser pulse is strong enough to nearly fully strip these atoms. The resulting plasma, therefore, has similar electron density, ions of similar  $Z$ , and a similar effective number of degrees of freedom.

The inclusion of the dopant is important, as the EOS has a measurable effect on the shock velocity and significantly increases the sensitivity to the conduction model. A flux-limited Spitzer-Harm electron conduction model is employed, with a value of the flux limiter of 0.06, consistent with accepted practices for similar systems [16,17]. This, paired with a scale factor on the laser energy to account for cross-beam

transfer and possibly other unmodeled loss mechanisms [18–20], constitutes the main points of uncertainty in the physics modeling. Both of these appear to be more critical for the direct drive than for the indirect drive, likely because the latter sees a hohlraum already filled with plasma, whose material properties have less-steep gradients and are evolving less quickly. Finally, a quiet-start option [21] was used to prevent unphysical interface motion prior to shock arrival.

We now demonstrate the copropagating shock, as well as the predictive capacity of the simulation. First, we examine the drive conditions via the radiation temperature as measured using the Dante [22] diagnostic. This is shown as a solid black curve in Fig. 3. From Fig. 3, the interior of the hohlraum heats to about 150 eV during the direct drive and then cools significantly while the lasers are off. Then, during the indirect drive, it heats back up to a peak temperature of about 175 eV. In the simulation, we model Dante by tallying the radiation flux away from the hohlraum at a location consistent with the Dante viewing angle. An effective radiation temperature is then estimated by fitting a Planckian function to the spectral flux distribution. The reported error accounts for the standard deviation of the fit, as well as the uncertainty in photon energy due to the finite width of the energy groups in the multigroup diffusion calculation.

The simulation does suffer from an unphysical stagnation feature inside the hohlraum, producing an axial jet that overtakes the second shock. This is a common feature in radiation-hydrodynamics simulations and is likely due to the fact that the continuum-fluid model used by the codes is not a good representation of the hot, low-density plasmas blowing off the walls of the hohlraum. The Knudsen number in this region tends to be large, and we expect the plasmas to interpenetrate kinetically rather than stagnate on axis [23]. We therefore choose to employ a workaround consisting of a smoothing algorithm. This algorithm homogenizes the plasma near the jet, easing the axial velocity and density of the jet, under the condition of conserving mass, momentum, and energy, which we judge to have the least impact on the driving conditions. We apply the homogenization twice, once at 8.5 ns and again at 15.5 ns.

The system downstream of the ablator takes one of two configurations, each optimized for complementary diagnostics. The first of these (the “VISAR” configuration) consists of a 50  $\mu\text{m}$ -thick layer of tungsten (an aluminum layer was also used but will not be analyzed here) behind the ablator, followed by a 1 mm-thick layer of  $\alpha$ -quartz ( $\text{SiO}_2$ ), as shown in Fig. 2(a). This permits the use of the line-imaging Velocity Interferometer System for Any Reflector (VISAR) [24,25]. VISAR produces a highly-resolved measurement of the leading shock velocity, allowing observation of the merger of our two shocks; data are shown in Fig. 4(a).

Because the quartz is initially transparent to the VISAR probe beam, the beam reflects off the tungsten until the shock breaks out of it, as seen by the sudden fringe shift and jump in signal marked by a “1” in the figure. The distortion seen in the half ns or so following the shock breakout is a result of shock refraction in the thin glue joint between the tungsten and quartz. Meanwhile, the merger of the second shock with the first, marked by a “1-2,” corresponds to a more subtle fringe shift but a clear jump in signal.

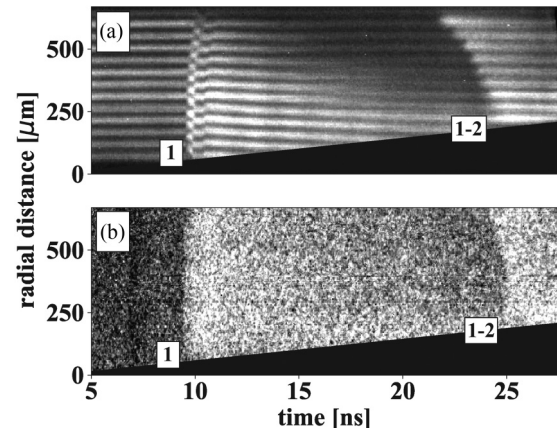


FIG. 4. (a) VISAR data for NIF shot N190415-001; (b) SOP data for the same shot. Breakout of the first, directly-driven shock (1) and the merging of this shock with the second, indirectly-driven shock (1-2) can clearly be seen by the disturbance these events produce on the VISAR fringes and the simultaneous jumps in thermal emission detected by the SOP. The blackened area corresponds to distorted data due to the axial seam [Fig. 2(a)].

Figure 4(b) shows data from the associated streaked optical pyrometer [26] (SOP), which records emission as a proxy for temperature and thus shock strength. SOP records little signal until the shock breaks out of the strongly-opaque, high-Z tungsten, and then suddenly begins to record the signal from the heated, shocked quartz. The signal slowly weakens as the shock (a blast wave) decays, until the second shock overtakes it and merges with it, increasing the temperature of the postshock state and therefore the self-emission.

From the shock breakout feature in Figs. 4(a) and 4(b), the two shock events are planar (to within the resolution of the feature) for a few hundred microns radially from the axis. One reason for the marginal planarity is a defect in coverage of the parylene coating of the hohlraum in the initial experiments, which we have since corrected. Further, coating of the ablator itself in undoped plastic will reduce the amount of iodine in the hohlraum fill, permitting more-uniform penetration of the indirect-drive laser beams. Both of these significantly enlarge the region of planar interface.

A well-resolved measurement of the shock velocity can be extracted from the shifting of the VISAR fringes [27] just outside the radius of the covered region in Fig. 4(a). The two VISAR legs, respectively, were set up with etalon thicknesses of 8.006 and 3.220 mm and vacuum velocities of 7.8001 and 19.3962 km/s/fringe. The probe beam had a wavelength of 660 nm, for which the refractive index of the quartz was 1.542. The result of this analysis is shown in Fig. 5. As in the raw data, the first shock breaks out of the tungsten and into the quartz at about 9.5 ns, with a velocity of about 23  $\mu\text{m}/\text{ns}$ . The shock speed slowly decays over the next several ns, until it is overtaken by the second shock at about 25 ns, and the velocity jumps from 16  $\mu\text{m}/\text{ns}$  up to about 21  $\mu\text{m}/\text{ns}$ . Notably, the first shock is a blast wave, consistent with the short duration of the direct-drive pulse, while the merged shock is steady, consistent with the prolonged, indirectly-driven radiation source in the hohlraum. This demonstrates some of the unique control

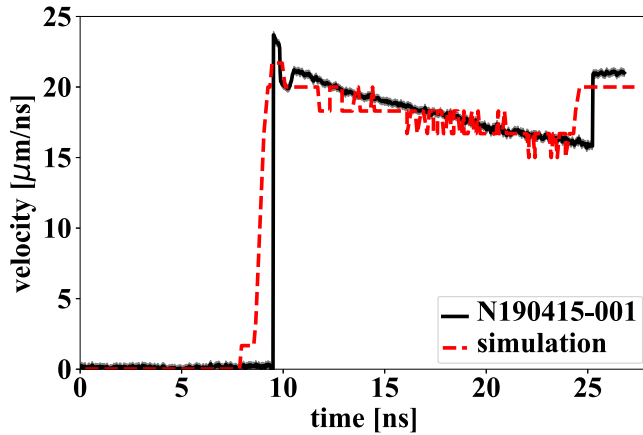


FIG. 5. Shock velocity measurement, starting when the shock breaks out of the W witness material, made using the VISAR diagnostic. The equivalent prediction from *xRAGE* calculations is also included. The two shock events can be clearly identified by the jumps in velocity at about 10 and 25 ns.

that we now have in the generation of multiple copropagating shocks in this experimental platform.

The simulated prediction is shown as a dashed red line in Fig. 5. According to the model, the shock breaks out of the tungsten at approximately the correct time, and the decaying shock velocity in the quartz is modeled well.

The second configuration (the “imaging” configuration), shown in Fig. 2(c), consists of a cylindrical piece of foamed polyethylene (density  $0.1 \text{ g/cm}^3$ ) placed downstream of the ablator and encased in a beryllium tube. This permits side-on radiography using the Big-Area Backlighter System [28]. Radiography is insensitive to details of the shock merger but gives visual information about the interface, similar to an eventual instability experiment. This experiment employs a “high” drive consisting of a simultaneous instead of sequential firing of the three subpulses (previously shown in Fig. 3), with all beams having the flat-top profile of the first one. This results in a shorter pulse—4 ns instead of 10 ns—but three times the intensity. This pulse also reduces optics damage to the laser system, by eliminating the tapered profile of the second and third subpulse. We choose to image the system at later times, such that we observe the largest possible difference in the relative positions of the shock and ablator features. These results are plotted in Fig. 6.

In the figure, the predicted interface and shock trajectories are plotted as a solid black line and dashed red lines, respectively, while experimental measurements of the interface and shock locations are plotted as black and red circles, respectively. The drive predictions, as benchmarked in detail by the VISAR experiment, are consistent with the experimental results in this configuration, giving us confidence that we have predicted reasonable hydrodynamics for each shock. For comparison, the predicted interface position in the absence of an indirect drive is shown as a dotted gray line—the slower trajectory would be measurably different.

The performance of the simulation in both configurations gives us confidence in our ability to predict flow physics produced by the shock. For the ablator/foam interface, about

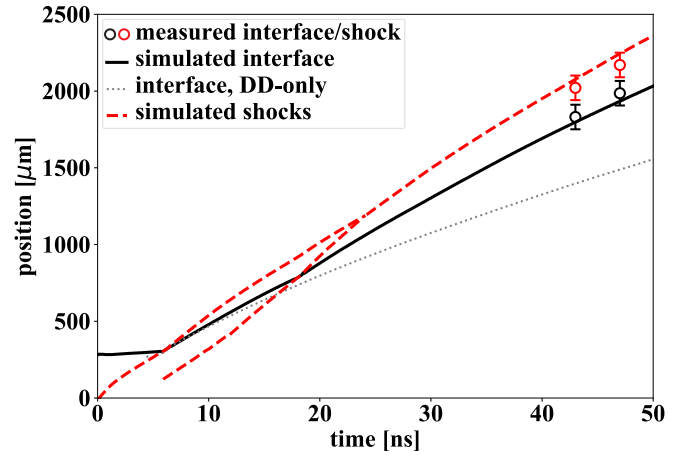


FIG. 6. Simulated interface and shock positions for the imaging system, shown as solid black and dashed red lines, respectively. The trajectory in the absence of the second, indirect drive is shown as a dotted gray line, and experimental data are shown as points. The second shock forms a few ns after the indirect pulse turns on and eventually merges with the first shock at about 23 ns. The predicted trajectory is consistent with the experimental measurement and would be measurably different in the absence of a second shock.

12 ns elapses between arrival of the first shock and second shocks. The first shock has a Mach number of about 6, with a pressure of about 8.7 Mbar, at the time it reaches the interface. The second shock arrives at the interface with a Mach number of about 1.5 and a pressure of around 3.5 Mbar, where the once-shocked plasma ahead of it has a pressure of about 1.5 Mbar. The pre- and postshock Atwood numbers at the interface are about 0.87/0.58 for the first shock and 0.45/0.5 for the second shock. These are approximately the conditions used to produce the example shown in Fig. 1, where machined interface structure with a wavelength of order tens of microns and initial amplitude of micron order are feasible [29] and compatible with the typical diagnostic resolution and timescales of these experiments.

In summary, we have produced two copropagating shocks across an unstable material interface, using a novel laser technique for the NIF. A crucial characteristic of our shocks is that they are independently controllable and are capable of carrying comparable amounts of energy. We have also shown that we are able to predict the shock behavior reasonably well using simulations performed with the *xRAGE* code. This gives us confidence in the computations as a design tool for future experiments studying reshocked interfacial instabilities. In the future, we will be able to tune the strength of the shocks and improve their planarity, both by removing the high-Z iodine dopant from the ablation plasma and by using a shorter pulse, and by controlling the intensity and timing shift of the indirect-drive pulse. Further, by using two halfraums, we can introduce a third and even a fourth counterpropagating shock into the system. This setup would preclude use of VISAR since the second halfraum would block the probe beam, but could be characterized using imaging radiography over the course of several shots. These possibilities open a new area of research into the physics of instability growth with copropagating shocks. As stated above, the physical

characteristics of copropagating versus counterpropagating shocks lead to significantly different behavior, which can now be theoretically validated, numerically modeled, and experimentally verified.

The authors would like to acknowledge the contributions of the MST-7 target fabrication team at LANL and the NIF Operations and Diagnostics teams, as well as useful

conversations with E. Dodd, P. Bradley, and J. Smidt. This work was supported by Los Alamos National Laboratory under Contract No. 89233218CNA000001 with Triad National Security, LLC. Part of this work was performed by Lawrence Livermore National Laboratory (LLNL) under Contract No. DE-AC52-07NA27344. Raw data were generated at the NIF at LLNL. Derived data supporting the findings of this study are available within the article.

- 
- [1] H. F. Robey, P. M. Celliers, J. L. Kline, A. J. Mackinnon, T. R. Boehly, O. L. Landen, J. H. Eggert, D. Hicks, S. Le Pape, D. R. Farley *et al.*, *Phys. Rev. Lett.* **108**, 215004 (2012).
- [2] G. Dimonte, C. E. Frerking, M. Schneider, and B. Remington, *Phys. Plasmas* **3**, 614 (1996).
- [3] S. R. Nagel, K. S. Raman, C. M. Huntington, S. A. MacLaren, P. Wang, M. A. Barrios, T. Baumann, J. D. Bender, L. R. Benedetti, D. M. Doane *et al.*, *Phys. Plasmas* **24**, 072704 (2017).
- [4] Y. Zhou, *Phys. Rep.* **723–725**, 1 (2017).
- [5] K. O. Mikaelian, *Phys. Rev. A* **31**, 410 (1985).
- [6] A. L. Velikovich, A. J. Schmitt, J. H. Gardner, and N. Metzler, *Phys. Plasmas* **8**, 592 (2001).
- [7] J. G. Wouchuk and K. Nishihara, *Phys. Rev. E* **70**, 026305 (2004).
- [8] F. W. Doss, J. L. Kline, K. A. Flippo, T. S. Perry, B. G. DeVolder, I. Tregillis, E. N. Loomis, E. C. Merritt, T. J. Murphy, L. Welsch-Sherrill, and J. R. Fincke, *Phys. Plasmas* **22**, 056303 (2015).
- [9] M. Gittings, R. Weaver, M. Clover, T. Betlach, N. Byrne, R. Coker, E. Dendy, R. Hueckstaedt, K. New, W. R. Oakes *et al.*, *Comput. Sci. Discov.* **1**, 015005 (2008).
- [10] D. Cao, G. Moses, and J. Delettrez, *Phys. Plasmas* **22**, 082308 (2015).
- [11] J. A. Marozas, M. Hohenberger, M. J. Rosenberg, D. Turnbull, T. J. B. Collins, P. B. Radha, P. W. McKenty, J. D. Zuegel, F. J. Marshall, S. P. Regan *et al.*, *Phys. Rev. Lett.* **120**, 085001 (2018).
- [12] B. M. Haines, D. Keller, J. Marozas, P. McKenty, K. Anderson, T. Collins, W. Dai, M. Hall, S. Jones, M. D. McKay, Jr., R. Rauenzahn, and D. Woods, *Comput. Fluids* **201**, 104478 (2020).
- [13] I. V. Igumenshchev, F. J. Marshall, J. A. Marozas, V. A. Smalyuk, R. Epstein, V. N. Goncharov, T. J. B. Collins, T. C. Sangster, and S. Skupsky, *Phys. Plasmas* **16**, 082701 (2009).
- [14] B. Bennett, J. Johnson, G. Kerley, and G. Rood, Recent Developments in the Sesame Equation-of-State Library, Technical Report LA-7130, Los Alamos National Laboratory (1978).
- [15] S. P. Lyon and J. D. Johnson, SESAME: The Los Alamos National Laboratory Equation of State Database, Technical Report LA-UR-92-3407, Los Alamos National Laboratory (1992).
- [16] S. X. Hu, V. A. Smalyuk, V. N. Goncharov, S. Skupsky, T. C. Sangster, D. D. Meyerhofer, and D. Shvarts, *Phys. Rev. Lett.* **101**, 055002 (2008).
- [17] R. P. Drake, *High-Energy-Density Physics*, 2nd ed. (Springer, Berlin, 2018).
- [18] I. V. Igumenshchev, D. H. Edgell, V. N. Goncharov, J. A. Delettrez, A. V. Maximov, J. F. Myatt, W. Seka, A. Shvydky, S. Skupsky, and C. Stoeckl, *Phys. Plasmas* **17**, 122708 (2010).
- [19] J. P. Sauppe, B. M. Haines, S. Palaniyappan, P. A. Bradley, S. H. Batha, E. N. Loomis, and J. L. Kline, *Phys. Plasmas* **26**, 042701 (2019).
- [20] O. S. Jones, C. A. Thomas, P. A. Amendt, G. N. Hall, N. Izumi, M. A. B. Garcia, L. F. B. Hopkins, H. Chen, E. L. Dewald, D. E. Hinkel *et al.*, *J. Phys.: Conf. Ser.* **717**, 012026 (2016).
- [21] B. M. Haines, C. H. Aldrich, J. M. Campbell, R. M. Rauenzahn, and C. A. Wingate, *Phys. Plasmas* **24**, 052701 (2017).
- [22] E. L. Dewald, K. M. Campbell, R. E. Turner, J. P. Holder, O. L. Landen, S. H. Glenzer, R. L. Kauffman, L. J. Suter, M. Landon, M. Rhodes, and D. Lee, *Rev. Sci. Instrum.* **75**, 3759 (2004).
- [23] L. F. Berzak Hopkins, S. Le Pape, L. Divol, N. B. Meezan, A. J. Mackinnon, D. D. Ho, O. S. Jones, S. Khan, J. L. Milovich, J. S. Ross *et al.*, *Phys. Plasmas* **22**, 056318 (2015).
- [24] R. M. Malone, J. R. Bower, D. K. Bradley, G. A. Capelle, J. R. Celeste, P. M. Celliers, G. W. Collins, M. J. Eckart, J. H. Eggert, B. C. Frogget *et al.*, *Proc. SPIE* **5580**, 505 (2005).
- [25] P. M. Celliers, D. K. Bradley, G. W. Collins, D. G. Hicks, T. R. Boehly, and W. J. Armstrong, *Rev. Sci. Instrum.* **75**, 4916 (2004).
- [26] J. E. Miller, T. R. Boehly, A. Melchior, D. D. Meyerhofer, P. M. Celliers, J. H. Eggert, D. G. Hicks, C. M. Sorce, J. A. Oertel, and P. M. Emmel, *Rev. Sci. Instrum.* **78**, 034903 (2007).
- [27] M. Millot, P. M. Celliers, P. A. Sterne, L. X. Benedict, A. A. Correa, S. Hamel, S. J. Ali, K. L. Baker, L. F. Berzak Hopkins, J. Biener *et al.*, *Phys. Rev. B* **97**, 144108 (2018).
- [28] K. Flippo, B. DeVolder, F. Doss, J. Kline, E. Merritt, E. Loomis, D. Capelli, D. Schmidt, and M. J. Schmitt, *J. Phys.: Conf. Ser.* **717**, 012062 (2016).
- [29] D. W. Schmidt, T. Cardenas, F. W. Doss, C. D. Stefano, P. M. Donovan, F. Fierro, K. A. Flippo, J. I. Martinez, and A. M. Rasmus, *Fusion Sci. Technol.* **73**, 474 (2018).